Taking advantage of multiplet structure for lineshape analysis in Fourier space

ADRIAN BECKERT,[1,2,4] HANS SIGG,[1] AND GABRIEL AEPPLI[1,2,3,5]

[1]*Laboratory for Micro and Nanotechnology, Paul Scherrer Institut, CH-5232 Villigen PSI, Switzerland*
[2]*Laboratory for Solid State Physics, ETH Zurich, CH-8093 Zurich, Switzerland*
[3]*Institute of Physics, EPF Lausanne, CH-1015 Lausanne, Switzerland*
[4]*adrian.beckert@psi.ch*
[5]*gabriel.aeppli@psi.ch*

Abstract: Lineshape analysis is a recurrent and often computationally intensive task in optics, even more so for multiple peaks in the presence of noise. We demonstrate an algorithm which takes advantage of peak multiplicity (N) to retrieve line shape information. The method is exemplified via analysis of Lorentzian and Gaussian contributions to individual lineshapes for a practical spectroscopic measurement, and benefits from a linear increase in sensitivity with the number N. The robustness of the method and its benefits in terms of noise reduction and order of magnitude improvement in run-time performance are discussed.

1. Introduction

Analysis of signal lineshapes is a prominent problem and a theme of importance in physics, chemistry and biomedicine. Ranging from spectroscopy [1–3] to scattering techniques [4–7], the lineshape can reveal underlying physical processes. For example, relaxation dynamics very commonly give rise to exponential decays in time which correspond in spectroscopy to Lorentzian peaks in frequency, while static disorder and instrumental effects typically induce Gaussian distributions of characteristic frequencies. Together, the two phenomena yield signal lineshapes which are convolutions of Lorentzians with Gaussians, objects referred to as Voigt lineshapes. The accurate parametrization of a Voigt lineshape retrieves the Lorentzian contribution, which, *e.g.*, quantifies correlation lengths in X-ray and neutron scattering [7] and coherence times of quantum systems in frequency-dependent spectroscopy [8–10]. The Gaussian part which is due to extrinsic factors such as grain size distribution in x-ray diffraction [6,11] and to spatial inhomogeneity in optical spectroscopy [2,12].

Approaches to lineshape determination (see [13] for an overview) deal with efficient numeric approximations [14,15] or tackle the deconvolution of single peaks in Fourier space [13,16,17], avoiding direct and computationally intensive Voigt profile fitting while allowing for correction of spurious frequencies. However, none of these numeric methods were applied in the context of multiplets, in spite of the numerous cases of finite-periodic signals, *e.g.*, for electronic multiplets of ions in solids [18], rotational spectra of molecules [19–21], neutron-scattering-resolved hyperfine interaction [22], X-ray diffraction of superlattices [23], and frequency combs [24,25]. Directly fitting a sum of profiles apparently exacerbates the problems of a direct single profile fit and would sacrifice the benefits (*e.g.*, computational speed-up) of Fourier space analysis. For well-separated profiles a split-up into single profiles may be a viable option, but misses an important feature of a combined analysis as we will show below.

In this article we extend previous work on single Voigt profile analysis [13,16,17] to multiplets and exploit the regular spacing for a robust and direct determination of the individual lineshape in Fourier space. Our method has multiple benefits. First, we exploit the speed of Fourier analysis while second, keeping the frequency-selective noise mitigation advantage from single-profile Fourier analysis. Third, the problem of multiplets becomes a benefit as we fit an exponential to the

envelope of the Fourier transform of the signal, which is parametrized only by the Lorentzian and Gaussian contributions to the individual line width. The method quantifies these contributions without the need for involved multi-Voigt profile analysis. Results are also readily checked by direct visual inspection of the Fourier transform. Furthermore, our method is computationally less expensive and its sensitivity increases linearly in N, the number of profiles. Although we focus on the common case of Voigt-shaped profiles, we expect our method will prove advantageous for other line-profiles, such as listed in reference [26].

We first derive the mathematical foundations of the method in section 2. In section 3 we apply the procedure to typical experimental data from solid-state spectroscopy, in this case a rare-earth doped crystal. Finally, in section 4 we discuss the method's performance when the initial assumption of finite-periodicity is relaxed.

2. Derivation of the method

We consider a real, finite-periodic signal $S(x) = \sum_i S_i(x)$, consisting of N profiles $S_i(x)$ spaced by Δx. We focus on the common cases of individual signal profiles $S_i(x)$ of Lorentzian, Gaussian and Voigt shapes. The general case for other classes of lineshapes is addressed subsequently.

2.1. Dirac delta model

For simplicity we first model $S(x)$ as a series of N Dirac delta functions $\delta(x)$, with N even, symmetrically distributed around $x = 0$. Definitions and a detailed derivation are in section A and B of the Appendix. The Fourier transform $\mathcal{F} : x \rightarrow k$ applied to the Dirac model $S_D(x)$ is given by

$$\mathcal{F}_D = \mathcal{F}[S_D(x)] = \frac{A}{\sqrt{2\pi}} \frac{\sin(N\Delta x k/2)}{\sin(\Delta x k/2)} \tag{1}$$

where A represents the integrated area of an individual signal profile. Without loss of generality, we restrict our analysis to $k \geq 0$. Figure 1 shows the amplitude spectrum $|\mathcal{F}_D|$, which exhibits a long periodicity $T_s = 2\pi/\Delta x$ modulated by a short periodicity $T_f = T_s/N$. Note the frequency doubling of $|\mathcal{F}_D|$ w.r.t $\mathcal{F}_D$. The occurrence of T_s in $|\mathcal{F}_D|$ stems from the regular spacing of the $S_i(x)$, and T_f from the length of the multiplet signal, which can be understood as the product of a rectangular window function with a Dirac comb (details in Appendix C) in analogy to the result of an $N-$periodic diffraction grating [27]. We denote the i-th maximum of $|\mathcal{F}_D|$ as $\mathcal{M}_i$, *i.e.* $|\mathcal{F}_D(i \times T_s)| = \mathcal{M}_i \; \forall i \in \mathbb{N}_0$. The inferior local maxima are labeled by $\mathcal{L}_j$. From Eq. (1) we obtain $\mathcal{M}_i \propto N$ for $\Delta x k/2 \mod \pi = 0$ with the rule of Bernoulli-de l'Hôspital and $\mathcal{L}_{j,\min} = 1/\sqrt{2\pi}$ does not depend on the multiplet number N. $\mathcal{M}_i \propto N$ represents the scaling of the sensitivity of our Fourier lineshape analysis (FLA) method.

For simplicity, we consider the modulus of $\mathcal{F}_D$ in this derivation to avoid the need for two exponential fits for positive and negative $\mathcal{M}_i$, as discussed in the following section and to allow for an application to more general cases as discussed in appendices E and F.

2.2. Lorentzian and Gaussian lineshapes

We now proceed to Lorentzian-shaped signal lines $S_i(x) = L(x)$, as illustrated in Fig. 2(a) and 2(b) for $N = 8$. The shape is given by

$$L(x, x_0, \Gamma, A) = \frac{A}{2\pi} \frac{\Gamma}{(x - x_0)^2 + \left(\frac{1}{2}\Gamma\right)^2} \tag{2}$$
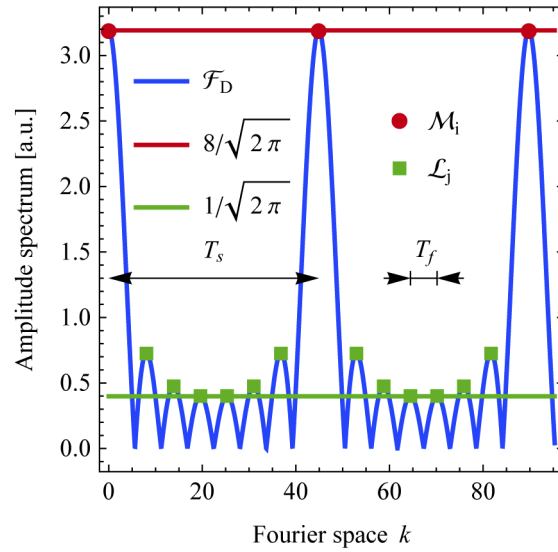
Fig. 1. Amplitude spectrum $|\mathcal{F}_D|$ of signal $S_D(x)$ for $N = 8$ and $A = 1$ (blue). The maxima $\mathcal{M}_i$ for $i \in \{1, 2, 3\}$ are marked in red and the inferior local maxima $\mathcal{L}_j$ in green. The uniformity of the amplitude of the $\mathcal{M}_i$ is highlighted by the constant red line at $8/\sqrt{2\pi}$, with spacing T_s and the minimal amplitude $\mathcal{L}_{j,\min}$ by the constant green line at $\sim 1/\sqrt{2\pi}$, spaced by T_f. The limits of $\mathcal{M}_i$ and $\mathcal{L}_{j,\min}$ are derived from Eq. (1).

with full-width-at-half-maximum (FWHM) Γ, center peak coordinate x_0 and integrated area $A = \int_{-\infty}^{\infty} L(x)\mathrm{d}x$. An N-fold repeated signal with spacing Δx is represented by

$$S_L(x) = \sum_{n=(1-N)/2}^{(N-1)/2} L(x, x_0 + n\Delta x, \Gamma, A) \tag{3}$$

and its Fourier transform $\mathcal{F}_L = \mathcal{F}[S_L(x)]$ as

$$\mathcal{F}_L = \exp\left(-\frac{1}{2}\Gamma k\right) \times \frac{A}{\sqrt{2\pi}} \frac{\sin(N\Delta x k/2)}{\sin(\Delta x k/2)} = \exp\left(-\frac{1}{2}\Gamma k\right) \times \mathcal{F}_D \tag{4}$$

for $x_0 = 0$. We see that $\mathcal{F}_L$ (Eq. (4)) differs from $\mathcal{F}_D$ (Eq. (1)) but by an exponentially decaying prefactor. Figure 3 visualizes this result for $N = 8$. The zero-order maximum $\mathcal{M}_0$ exhibits the same amplitude from Eq. (1) but for $i > 0$ the amplitudes $\mathcal{M}_i$ decay with $E_L(k) = \exp(-\frac{1}{2}\Gamma k)$ and the sensitivity $\mathcal{M}_i \propto N$ of $\mathcal{F}_D$ still holds. In the same way we obtain, for a Gaussian model $S_G(x)$,

$$\mathcal{F}_G = \mathcal{F}[S_G(x)] = \exp\left(-\frac{1}{2}\sigma^2 k^2\right) \times \mathcal{F}_D \tag{5}$$

which again exhibits the same periodicity T_s as Eq. (1) and Eq. (4). The exponential prefactor defining the envelope $E_G(k)$ of $\mathcal{F}_G$ is now given by $E_G(k) = \exp(-\frac{1}{2}\sigma^2 k^2)$. The amplitude reduction of $\mathcal{M}_i$ for $i > 0$ thus depends on σ which is related to the Gaussian FWHM

$$f_G = 2\sqrt{2\ln(2)}\sigma. \tag{6}$$

2.3. Voigt profile model

The Voigt lineshape $V(x)$ is defined as the convolution ($*$) of a Lorentzian with a Gaussian function

$$V(x) = L(x) * G(x) = \int_{-\infty}^{\infty} L(x')G(x - x')\mathrm{d}x' \tag{7}$$

and equivalently

$$S_{\mathrm{V}}(x) = \sum_{n=(1-N)/2}^{(N-1)/2} V(x, x_0 - n\Delta x, \Gamma, \sigma, A). \tag{8}$$
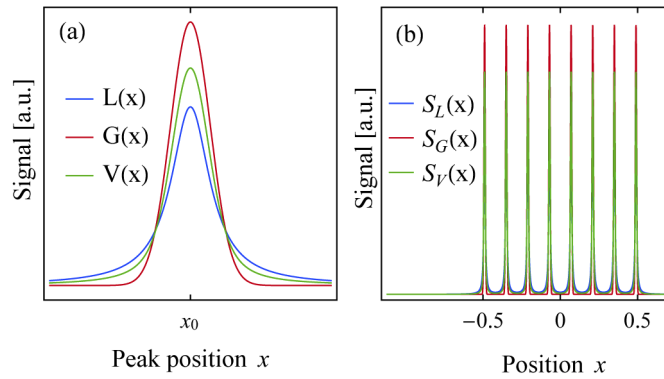

Fig. 2. Signal $S(x)$ lineshape illustrations. (a) Lorentzian $L(x)$ (blue), Gaussian $G(x)$ (red) and Voigt $V(x)$ (green) lineshape with identical center x_0, area and FWHM. (b) Sum of eight equally-spaced Lorentzian $L(x)$, Gaussian $G(x)$ and Voigt $V(x)$ profiles, each with identical area and FWHM.
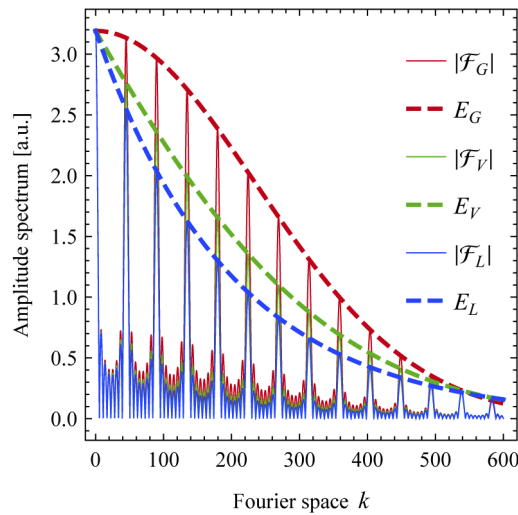

Fig. 3. Fourier transform of the signal functions shown in Fig. 2(b). $|\mathcal{F}_{\mathrm{L}}|$ (blue), $|\mathcal{F}_{\mathrm{G}}|$ (red) and $|\mathcal{F}_{\mathrm{V}}|$ (green). The first few $\mathcal{M}_i$ are depicted for all three cases, together with the envelopes (dashed) defining their amplitudes.

We find for $\mathcal{F}_V = \mathcal{F}[S_V(x)]$ (*c.f.* Appendix D)

$$\mathcal{F}_V = \exp\left[-\frac{1}{2}\left(\Gamma + \sigma^2 k\right)k\right] \times \mathcal{F}_D \tag{9}$$

and observe that the sensitivity $\mathcal{M}_i \propto N$ still holds. Due to the convolution theorem the envelope $E_V(k)$ defining the amplitudes of the $\mathcal{M}_i$ is given by

$$E_V(k) = E_L(k)E_G(k) = \exp\left[-\frac{1}{2}\left(\Gamma + \sigma^2 k\right)k\right] \tag{10}$$

which is only parametrized by the Lorentzian line width Γ and the Gaussian σ. For illustration, Fig. 3 shows this for $N = 8$, in addition to the Lorentzian and Gaussian cases. The Voigt FWHM f_V can be approximated with an accuracy of 0.02% [28] by

$$f_V = 0.5346 f_L + \sqrt{0.2166 f_L^2 + f_G^2} \tag{11}$$

where $f_L \equiv \Gamma$.

Given a finite-periodic signal $S(x)$ consisting of N Voigt-profile peaks $S_i(x)$, spaced by Δx, the line width contributions Γ, σ of the individual signal peaks $S_i(x)$ can thus be determined by fitting $E_V(k)$ to the $\mathcal{M}_i$, allowing to distinguish the Lorentzian contribution to the line width from that due to the Gaussian. From Eq. (9) and Fig. 3 the behavior of $\mathcal{F}_V$ is dominated by $E_L(k)$ for small k and by $E_G(k)$ for large k, which allows for a quick qualitative analysis of the Lorentzian contribution by examination of the first few $\mathcal{M}_i$ - even by eye. In principle this applies also to the strong suppression or the slow decay of the tail by $E_G(k)$ and $E_L(k)$ respectively, but might not be unambiguously determined due to noise.

2.4. Sensitivity and generalization of the method

The Fourier transform simplifies the convolution integral to a product and thus, the number of profiles can be understood as the number of terms of a discrete Fourier transform leading to a linear increase of the sensitivity, proportional to N (see Eq. (20) in the Appendix). This is analogous to the $N-$periodic diffraction grating; the $\mathcal{M}_i$ become more expressed and sharpen as N increases with the limit of becoming the Dirac comb for $N \rightarrow \infty$. This allows us to extract values for $\mathcal{M}_i$ even if $\mathcal{L}_j$ is below the noise level in the experimental setup. Thus, our result is particularly interesting for experimental applications where N is large (*e.g.*, [21], $N>60$) and the $\mathcal{M}_i$ best expressed. The case for small N or even $N = 1$ (*c.f.* Ref. [13,17]) is possible, but exhibits eventually vanishing advantage from the sensitivity scaling with N. We note that the FLA method exhibits a particular strength for applications to measurement resolution-limited spectra. With constant resolution and increasing N, the resolution of $\mathcal{F}_D$ in $k-$space and thus the precision of the $\mathcal{M}_i$ is increased. However, increasing the resolution of a single-peak measurement does not increase the number of $\mathcal{M}_i$ usable for the envelope fit, but extends $\mathcal{F}_D$ further in $k-$space (*c.f.* Fig. 4(b)).

Thanks to the simplification of the convolution integral and the scaling of the sensitivity with N, our method should be as beneficial when applied to other classes of convolved line profiles [26] as for the Voigt profile. The accuracy for each case would, however, need to be separately analyzed.
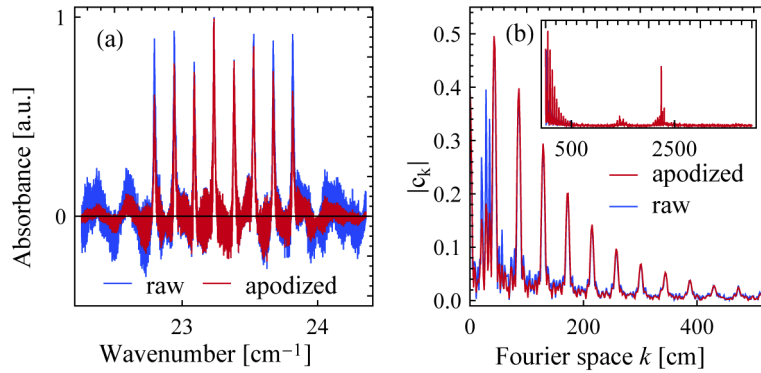
Fig. 4. (a) Unapodized and apodized absorbance spectrum of $LiY_{1-x}Ho_xF_4$ ($x = 0.3\%$) with 0.001 cm^{-1} resolution at a temperature T = 3.8 K, exhibiting an eightfold repeated signal due to the I = 7/2 nuclear hyperfine levels of the Ho atoms. The BH4T apodization function is centered at the spectrum and decays to zero on its ends. (b) DFT coefficient $|c_k|$ of data shown in (a). Inset: The characteristic pattern decays within the first 600 Fourier components. Around $k = 1440$ and $k = 2240$ there are strong noise contributions from Fabry-Perot interference due to reflecting optical components.

3. Example

In this section we demonstrate the application of the proposed method to a multiplet signal, which in this case is a typical absorbance spectrum measured in transmission for a $LiY_{1-x}Ho_xF_4$ single crystal with $x = 0.3\%$ at a temperature T of 3.8 K with a Fourier transform infrared (FTIR) spectrometer. The Bruker IFS125 spectrometer is based at the infrared beamline of the Swiss Light Source at Paul Scherrer Institut in Villigen, Switzerland [29]. The spectrum in Fig. 4(a) shows the hyperfine-split ground state to second excited state transition at ~ 23.3 cm^{-1} (700 GHz) in spectroscopic units [cm^{-1}]. Thanks to the ultra-high resolution FTIR in combination with the highly collimated, high-brillance infrared beam we achieved 0.001 cm^{-1} (30 MHz) resolution, corresponding to 4779 measurement points in total and ~ 16 points per individual peak width. We refer to Matmon *et al.* [18] for details on the general experimental setup and FTIR technique as well as for more extensive, spectroscopic work on $LiY_{1-x}Ho_xF_4$. The FLA method is ideal for analysis of multiple spectra as a function, *e.g.*, of temperature as in the latter case, thanks to its efficiency.

3.1. Procedure

Equation (9) leads to an algorithmic procedure for extracting the shape and line width of a finite-periodic signal:

1. Calculate the Fourier transform of the finite-periodic signal and take the modulus.

2. Determine the maxima $\mathcal{M}_i$ defining the envelope $E_V(k)$, which occur with periodicity T_s.

3. Fit the envelope function

$$E_V(k, \Gamma, \sigma, P, c) = P \times \exp\left[-\frac{1}{2}\left(\Gamma + \sigma^2 k\right) k\right] + c \tag{12}$$

   to the $\mathcal{M}_i$.

We replace the analytical prefactor $|\mathcal{F}_D|$ of the envelope with P as the global scaling factor, combining factors from the normalization of the Fourier transform, the single signal line area

A and experimental sensitivities. The offset constant *c* accounts for nonzero white noise in the experiment. We note that if Δx is known, the $\mathcal{M}_i$ might be more precisely determined thanks to $T_s = 2\pi/\Delta x$. This simple procedure allows for algorithmic implementation.

3.2. Application to experimental data

We apply the above procedure to the transmission spectrum in Fig. 4(a). More details on the numerical discrete Fourier transform (DFT) procedure are found in the Appendix G. Figure 4(b) shows the modulus of the DFT coefficients c_k of the unapodized (blue) and apodized (red) spectrum (details of apodization are in Appendix G) in Fig. 4(a) for $k<600$. The characteristic pattern of Eq. (9) is evident in Fig. 4. The inset displays all Fourier coefficients. We observe reduced noise frequencies in k-space in Fig. 4(b) for the apodized spectrum and a different global scaling factor P with respect to the unapodized spectrum. However, the decay constants Γ, σ are unchanged.

Figure 5 shows the DFT of the apodized spectrum and the $\mathcal{M}_i$. We apply a simple algorithm detecting the evenly-spaced maxima $\mathcal{M}_i$ with period $T_s \sim 45$ Fourier coefficients. We set a conservative threshold at $k = 520$ to ensure a fiducial selection of the $\mathcal{M}_i$. We drop $\mathcal{M}_0$ as it is strongly affected by the Fourier transforms zero center peak. The result of the envelope $E(\Gamma, \sigma, P)$ fit for a Lorentzian, Gaussian and Voigt lineshape to the $\mathcal{M}_i$ is displayed in Fig. 5. We observe that the Voigt profile yields the largest $R^2 = 0.998$ value and at least two times smaller residuals in comparison to the pure Gaussian or Lorentzian profile. The fit results are $\Gamma = 1.1 \times 10^{-2} \pm 0.12 \times 10^{-3}$ cm^{-1} and $\sigma = 3.5 \times 10^{-3} \pm 0.6 \times 10^{-3}$ cm^{-1} with uncertainties being standard parameter estimation errors obtained by covariance matrix. With Eq. (6) we find $f_G = 8.5 \times 10^{-3} \pm 1.4 \times 10^{-3}$ cm^{-1} and with Eq. (11) $f_V = 15.7 \times 10^{-3} \pm 1.6 \times 10^{-3}$ cm^{-1}. The same values within the fit precision are obtain by a direct Voigt profile fit to the individual signal peaks. The method determines that f_L, the Lorentzian part of the line width, is the slightly larger contribution.
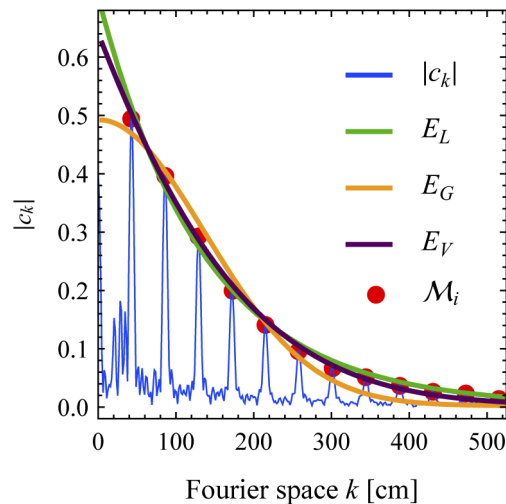

Fig. 5. Modulus of Fourier coefficients of apodized spectrum in Fig. 4(a) (blue). Red points denote the selected $\mathcal{M}_i$. Solid lines represent the envelope fit.

4. Robustness, noise stability and run time

We discuss the robustness of the method under deviations to the initial assumption of regular spacing and compare its performance to a direct least-squares fit method (DFM).

4.1. Robustness

In the case of unequal areas A_i, the individual areas A_i of the signal lines appear as an overall scaling factor (derivation in Appendix E) which is already considered in section 3. This allows the application of the method in cases where the individual signal line varies strongly in intensity *e.g.* for rotational/vibrational spectra [21]. The extracted line width in case of differing individual line widths Γ_i, σ_i is a weighted average (*c.f.* Appendix F).

As regular spacing is the underlying assumption, a variation of the line spacing Δx directly modifies the $\mathcal{M}_i$ and thus the observed envelope $E(\Gamma, \sigma, P)$. Because of the line spacing variation the N frequencies exhibit phase differences resulting in destructive interference and less expressed $\mathcal{M}_i$ (*c.f.* Appendix B). This leads to an overestimation of the width and deviation from actual profile shape. We note that a second order hyperfine interaction in the example spectrum (for details see [18]) results in a 2.7 % deviation from equidistancy of the eight hyperfine lines. Nevertheless we obtain equivalent results for line width and shape, showing the robustness of the method against small (on the scale of $\lesssim \Delta x/N$) relaxation in finite-periodicity of $\lesssim 3\%$. Furthermore, if the variations Δx_i are known, then $E(\Gamma, \sigma, P)$ could be adjusted to depend on the Δx_i.

4.2. Noise-stability

The noise spectrum is explicitly revealed with the FLA method. In case of a few isolated frequencies, as in *e.g.* the inset in Fig. 4, the noise does not affect the envelope fit in k-space and the method naturally implements a low-pass frequency filter. A particular strength of the method comes from the possibility to fade out noisy peaks that occur at frequencies between the $\mathcal{M}_i$ as is the case in Fig. 4 at *e.g.* $k = 70$. Such noise peaks will affect the DFM results and low-pass filters can not be applied. Consideration only of $\mathcal{M}_i$ for the envelope fit provides an inherent and impartial filter of the associated noise.

Assuming Gaussian RMS noise for artificial spectra with up to 50% of the signal amplitude, we find the FLA method to be comparable to DFM within the statistical parameter errors (*c.f.* Appendix H). This holds true for different ratios of $\Gamma/\sigma \in 0.1, 1, 10$. We find that the precision for both, FLA and DFM strongly decreases for $\Gamma/\sigma < 0.1$ and $\Gamma/\sigma > 10$. We observe a systematic error for the FLA method in the form of an increase of the Gaussian line width contribution with increasing RMS noise amplitude. We attribute this to the fact that our analysis in Fourier space reflects the noise spectrum convolved with the signal and thus adds to the Gaussian line width contribution. Although the DFM method may occasionally exhibit a more precise performance, the FLA method extracts line width and shape information algorithmically, with less computational power and fewer data points, as detailed in the next subsection.

4.3. Run time

We note the significantly different computational intensity of both methods. On our system (Intel Xeon E5-2670 0 @2.6 GHz, 2 processors with 192 GB usable RAM) DFM is at least one to two orders of magnitude slower than the FLA method. A test on 1000 data sets with $N = 8$ peaks, 1000 data points, and varying Gaussian RMS noise yielded 1.6 s run time for the FLA method and 2543 s for DFM. Runtimes are dataset specific and further (algorithm) optimization may reduce the run time discrepancy. For fundamental reasons, however, a run time difference will persist as the FLA method allows to reduce the parameter space to four (Γ, σ, P, c), whereas a direct fit method has to consider at least six $(\Gamma, \sigma, \text{area } A, \text{position } x_0, \text{spacing } s, \text{offset } c)$ under the assumption of identical areas A_i, which is rarely fulfilled. Any individual consideration of a parameter in the direct fit scales the parameter space with N. This increases the run time for the DFM method significantly. Furthermore, the final envelope fit is performed on a fraction of the initial data points. In case of insufficient precision of the FLA method, it may well serve as a fast pre-analysis for good DFM start parameters.

5. Conclusion

We have introduced and demonstrated a method of extracting the line-width and shape of a multiplet signal. The basic idea and mathematics are actually straightforward generalizations of the Debye-Waller effect [30] in scattering techniques, where the intensities of Bragg peaks shrink with increasing order in proportion to an envelope function decaying as a Gaussian whose width in reciprocal space is inversely proportional to the uncertainty in the positions of the atoms in real space. We offer a direct and computationally efficient way of quantifying the Lorentzian and Gaussian parts of multiple Voigt profiles by harnessing the regular spacing of the signal. The method benefits from a linear increase in sensitivity with the number of profiles of the multiplet. Furthermore, we highlighted that the FLA method is comparable to a direct least square fit, but is less computationally intensive and exhibits significant advantages in the presence of low-frequency noise. Finally, the FLA method might serve as a fast and algorithmic pre-analysis for starting parameter determination cases where the assumption of periodic repetition of the same lineshape is broken. Potential applications are ample. X-ray scattering may benefit where quasiperiodic structures are sampled within finite real space windows for problems such as integrated circuit microscopy [31,32]. Our method could also be applied to optical comb-based spectroscopies [24] for precision measurements in atomic and solid-state physics.

Appendix

A. Definitions

The Fourier transform we use throughout the article is defined as

$$\mathcal{F}[S(x)] = 1/\sqrt{2\pi} \int_{-\infty}^{\infty} S(x)\exp[-ikx]dx. \tag{13}$$

We use the following definition of a Dirac comb III:

$$\mathrm{III}_{\Delta x}(x) = \frac{1}{\Delta x}\mathrm{III}\left(\frac{x}{\Delta x}\right) = \sum_{n=-\infty}^{\infty} \delta(x - n\Delta x) \tag{14}$$

where $\delta(x)$ denotes the Dirac delta function. The Fourier series of the Dirac comb is given by

$$\mathrm{III}_{\Delta x}(x) = \frac{1}{\sqrt{2\pi}}\sum_{n=-\infty}^{\infty}\exp(-ikn\Delta x) = \frac{1}{\sqrt{2\pi}}\left[1 + 2\sum_{n=1}^{\infty}\cos(kn\Delta x)\right] \tag{15}$$

which directly yields another interpretation of Eq. (1): It is the sum of the first N terms of the Fourier series of the Dirac comb $\mathrm{III}_{\Delta x}(x)$ for odd N.

The rectangular window function of height h and width w is defined as

$$\mathrm{rect}(h, w) = h \times \mathrm{rect}\left(\frac{x}{w}\right) \tag{16}$$

where we use the standard definition for the unit rectangular function $\mathrm{rect}(x) = 1 \; \forall x \in \{-1/2, 1/2\}$ and 0 otherwise.

The model where the individual signal peaks $S_i(x) = G(x)$ are Gaussian (*c.f.* Fig. 2(a) and (b)) is given by

$$S_G(x) = \frac{A}{\sqrt{2\pi}\sigma}\sum_{n=(1-N)/2}^{(N-1)/2}\exp\left[-\frac{(x - x_0 - n\Delta x)^2}{2\sigma^2}\right] \tag{17}$$

with standard deviation σ, center signal line position x_0, spacing Δx and integrated area A. The Fourier transform of $S_G(x)$ (with $x_0 = 0$) is given by

$$\mathcal{F}_G = \mathcal{F}[S_G(x)] = \exp\left(-\frac{1}{2}\sigma^2 k^2\right)\mathcal{F}_D. \tag{18}$$

B. Detailed derivation

The Dirac model $S_{\mathrm{D}}(x)$ is given by

$$S_{\mathrm{D}}(x) = A \sum_{n=(1-N)/2}^{(N-1)/2} \delta(x - n\Delta x) \tag{19}$$

assuming symmetry around $x = 0$. With $\{A, n, \Delta x, k\} \in \mathbb{R}$ we obtain for $\mathcal{F}_{\mathrm{D}}$

$$\mathcal{F}_{\mathrm{D}} = \frac{1}{\sqrt{2\pi}} \int_{-\infty}^{\infty} A \sum_{n=(1-N)/2}^{(N-1)/2} \delta(x - n\Delta x) \times \exp(-ikx) \, \mathrm{d}x = \frac{A}{\sqrt{2\pi}} \sum_{n=(1-N)/2}^{(N-1)/2} \exp(-ikn\Delta x) \tag{20}$$

which, for N even yields

$$\mathcal{F}_{\mathrm{D}} \stackrel{N \text{ even}}{=} \frac{A}{\sqrt{2\pi}} \sum_{n=1/2}^{(N-1)/2} \exp(-ikn\Delta x) + \exp(ikn\Delta x) = A\sqrt{\frac{2}{\pi}} \sum_{n=1/2}^{(N-1)/2} \cos(n\Delta x k) \tag{21}$$

and for odd N

$$\mathcal{F}_{\mathrm{D}} \stackrel{N \text{ odd}}{=} \frac{A}{\sqrt{2\pi}} \sum_{n=0}^{(N-1)/2} \exp(-ikn\Delta x) + \exp(ikn\Delta x) = A\sqrt{\frac{2}{\pi}} \left[\frac{1}{2} + \sum_{n=0}^{(N-1)/2} \cos(n\Delta x k) \right] \tag{22}$$

For even N we further use

$$\begin{aligned}
\sum_{n=1/2}^{(N-1)/2} \cos(n\Delta x k) &= \sum_{n=0}^{N/2-1} \cos\left[\left(n + \frac{1}{2} \right) \Delta x k \right] = \sum_{n=0}^{N/2-1} \mathrm{Re} \left\{ \exp\left[i \left(n + \frac{1}{2} \right) \Delta x k \right] \right\} \\
&= \mathrm{Re} \left[\exp\left(\frac{i\Delta x k}{2} \right) \sum_{n=0}^{N/2-1} \exp\left(in\Delta x k \right) \right] = \mathrm{Re} \left[\exp\left(\frac{i\Delta x k}{2} \right) \frac{1 - \exp(iN\Delta x k/2)}{1 - \exp(i\Delta x k)} \right] \\
&= \mathrm{Re} \left[\exp\left(\frac{iN\Delta x k}{4} \right) \frac{\exp\left(-\frac{iN\Delta x k}{4} \right) - \exp\left(\frac{iN\Delta x k}{4} \right)}{\exp\left(-\frac{i\Delta x k}{2} \right) - \exp\left(\frac{i\Delta x k}{2} \right)} \right] \\
&= \frac{\cos(N\Delta x k/4)\sin(N\Delta x k/4)}{\sin(\Delta x k/2)} = \frac{1}{2} \frac{\sin(N\Delta x k/2)}{\sin(\Delta x k/2)}
\end{aligned} \tag{23}$$

and we leave the case for the odd N to the reader. From Eq. (21) we conclude that

$$\mathcal{F}_{\mathrm{D}} = \frac{A}{\sqrt{2\pi}} \frac{\sin(N\Delta x k/2)}{\sin(\Delta x k/2)} \quad \forall N \geq 2 \in \mathbb{N}. \tag{24}$$

Equation (24) shows that the number of signal lines N of $S(x)$ determines the amplitude of the $\mathcal{M}_i = NA/\sqrt{2\pi} \; \forall i$. This is determined with the rule of Bernoulli-de l'Hôspital where numerator $[\sin(N\Delta x k/2)]$ and denominator $[\sin(\Delta x k/2)]$ vanish which is the case for $\Delta x k/2 \bmod \pi = 0$. Furthermore, $\mathcal{L}_j \sim A/\sqrt{2\pi} \; \forall j$ as $\mathcal{L}_{j,\mathrm{min}}$ denotes the point where numerator and denominator are equal to one. Note that for even N this condition is never exactly met and $\mathcal{L}_{j,\mathrm{min}}$ slightly smaller than 1 but still independent of N. These results lead to

$$\frac{\mathcal{M}_i}{\mathcal{L}_{j,\mathrm{min}}} \propto N \tag{25}$$

which is the scaling of the sensitivity of the FLA method with the number N of individual signal profiles $S_i(x)$, in analogy to a finite diffraction grating. This result can be alternatively understood as the approximate ratio of the main maximum to the first side lobe of a sinc-function, as shown in the next subsection.

C. Alternative derivation

A sum of N delta functions centered around 0 and spaced by Δx can be written as

$$S_{\mathrm{D}}(x) = A \sum_{n=(1-N)/2}^{(N-1)/2} \delta(x - n\Delta x) \ \forall N \in \mathbb{N} \geq 2 \tag{26}$$

or as

$$S_{\mathrm{D}}(x) = A\mathrm{III}_{\Delta x}(x)\mathrm{rect}\left(\frac{x}{N\Delta x}\right) \ \forall N \in \mathbb{N} \geq 2 \tag{27}$$

For $\mathcal{F}[S_{\mathrm{D}}(x)] \equiv \mathcal{F}_{\mathrm{D}}$ follows with the application of the convolution theorem:

$$
\begin{aligned}
\mathcal{F}_{\mathrm{D}} &= A\mathcal{F}\left[\mathrm{III}_{\Delta x}(x)\mathrm{rect}\left(\frac{x}{N\Delta x}\right)\right] = A\mathcal{F}\left[\mathrm{III}_{\Delta x}(x)\right] * \mathcal{F}\left[\mathrm{rect}\left(\frac{x}{N\Delta x}\right)\right] \\
&= \frac{A}{\Delta x}\mathrm{III}_{\frac{1}{\Delta x}}(k) * \frac{N\Delta x}{\sqrt{2\pi}}\mathrm{sinc}\left(\frac{N\Delta x}{2}k\right) = \frac{AN}{\sqrt{2\pi}}\sum_{m=-\infty}^{\infty}\mathrm{sinc}\left[\frac{N\Delta x}{2}\left(k - \frac{m}{\Delta x}\right)\right]
\end{aligned}
\tag{28}
$$

which reveals Eq. (1) to be an infinite sum of sinc functions.

D. Detailed derivation of Voigt model

We present the detailed derivation for $\mathcal{F}_{\mathrm{V}}$.

$$
\begin{aligned}
\mathcal{F}_{\mathrm{V}} &= \mathcal{F}\left[\sum_{n=(1-N)/2}^{(N-1)/2} V(x, x_0 - n\Delta x, \Gamma, \sigma, A)\right] = \sum_{n=(1-N)/2}^{(N-1)/2} \mathcal{F}\left[V(x, x_0 - n\Delta x, \Gamma, \sigma, A)\right] \\
&= \sum_{n=(1-N)/2}^{(N-1)/2} \mathcal{F}\left[L(x, x_0 - n\Delta x, \Gamma, A) * G(x, 0, \sigma, 1)\right] \\
&= \sum_{n=(1-N)/2}^{(N-1)/2} \mathcal{F}\left[L(x, x_0 - n\Delta x, \Gamma, A)\right] \times \mathcal{F}\left[G(x, 0, \sigma, 1)\right]
\end{aligned}
\tag{29}
$$

which for $x_0 = 0$ simplifies to

$$
\begin{aligned}
\mathcal{F}_{\mathrm{V}} &= \frac{A}{\sqrt{2\pi}}\sum_{n=(1-N)/2}^{(N-1)/2}\exp\left(ikn\Delta x - \frac{1}{2}\Gamma\right) \times \exp\left(-\frac{1}{2}\sigma^2 k^2\right) \\
&= \frac{A}{\sqrt{2\pi}}\sum_{n=(1-N)/2}^{(N-1)/2}\exp\left[ikn\Delta x - \frac{1}{2}(\Gamma + k\sigma^2)k\right] \\
&= \frac{A}{\sqrt{2\pi}}\exp\left[-\frac{1}{2}(\Gamma + k\sigma^2)k\right]\sum_{n=(1-N)/2}^{(N-1)/2}\exp(ikn\Delta x) \\
&\stackrel{N \text{ even}}{=} A\sqrt{\frac{2}{\pi}}\exp\left[-\frac{1}{2}(\Gamma + k\sigma^2)k\right]\sum_{n=1/2}^{(N-1)/2}\cos(kn\Delta x).
\end{aligned}
\tag{30}
$$

We leave the case of odd N to the reader.

E. Relaxation of identical area

We derive the general case for varying areas A_n by using $|z|^2 = z \times \bar{z}$

$$|\mathcal{F}_D|^2 = \frac{1}{2\pi} \sum_{n_1=(1-N)/2}^{(N-1)/2} A_{n_1} \exp(-ikn_1\Delta x) \sum_{n_2=(1-N)/2}^{(N-1)/2} A_{n_2} \exp(ikn_2\Delta x) \tag{31}$$

and using Euler's formula in combination with trigonometric identities we find

$$2\pi|\mathcal{F}_D|^2 = \sum_{n_1,n_2} A_{n_1}A_{n_2} \left[\cos(kn_1\Delta x)\cos(kn_2\Delta x)\sin(kn_1\Delta x)\sin(kn_2\Delta x)\right]$$

$$= \sum_{n_1,n_2} \cos[k(n_1-n_2)\Delta x] = \sum_{m=0}^{N-1} B_m\cos(km\Delta x) \tag{32}$$

by collecting identical $n_1 - n_2 = m$. Depending on the parity of N this equals Eq. (21) or Eq. (22), except for the $m-$dependent prefactor $B_m \approx \bar{A}(N-m)$, $\bar{A}$ denoting the average of all A_n. The occurrence of $\mathcal{M}_i$ is characterized by $\Delta x k/2 \bmod \pi = 0$, with amplitude $\sum_{m=0}^{N-1} B_m$. The amplitude of the inferior maximum $\mathcal{L}_i$ of order l is maximally $\sum_{i=l}^{N-1} B_m$, showing that the main characteristics of Eq. (23) and therefore Eq. (1) is conserved for the general case, differing only in amplitude of the $\mathcal{M}_i$ and modified behavior of $|\mathcal{F}_D|$ around the zeros.

F. Relaxation of identical line width and shape

We start from Eq. (29) treating the general case of varying Γ_n, σ_n

$$\mathcal{F}_V = \frac{A}{\sqrt{2\pi}} \sum_{n=(1-N)/2}^{(N-1)/2} \exp(ikn\Delta x) \times \exp\left[-\frac{1}{2}\left(\Gamma_n + k\sigma_n^2\right)k\right] \tag{33}$$

observing the closeness to previous section E, with

$$A_n = \exp\left[-\frac{1}{2}\left(\Gamma_n + k\sigma_n^2\right)k\right] \tag{34}$$

allowing us to reduce this case to the previous one. Here we observe that $\sum_{m=0}^{N-1} B_m$ is the (weighted) sum over the different line widths and shapes (in the general case).

G. Details on numerical Fourier transform and apodization

Prior to the Fourier transform, the application of an apodization function to the spectrum is recommended. High frequency noise and distortion effects of lineshapes due to the DFT on finite-sized signals are minimized. The red trace in Fig. 4(a) is apodized by a 4 cm^{-1} wide Blackman-Harris 4-term (BH4T) apodization function [33,34], centered at 23.3 cm^{-1}. The unit width BH4T(x) function $-1/2 \leq x \leq 1/2$ is defined as

$$\text{BH4T}(x) = 0.035875 + 0.48829 \times \cos(2\pi x) + 0.14128 \times \cos(4\pi x) + 0.0.01168 \times \cos(6\pi x) \tag{35}$$

and BH4T(x) $= 0 \; \forall \; |x| > 1/2$ [34].

H. RMS noise test

For the RMS noise test we create artificial data, where we add different amplitudes of RMS noise and apply the FLA as well as the DFM method with a Voigt lineshape model, for the case of $N = 8$ peaks. The results are shown in Fig. 6. Gridlines denote the initial values before RMS noise application. For contribution ratios $\Gamma/\sigma = 0.1$ the FLA method tends to overestimate the overall line width. We attribute this to a systematic error, which pushes the ratio in the limit where the methods precision strongly decreases.
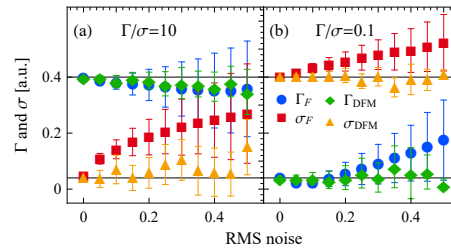
Fig. 6. RMS noise test. (a) Extracted fit results Γ_F, σ_F for $\Gamma/\sigma = 10$ under RMS noise with the FLA method and direct least-squares fit ($\Gamma_{\text{DFM}}, \sigma_{\text{DFM}}$). Gridlines denote the initial values before RMS noise application (b) Same as (a) with inverse contribution ratio $\Gamma/\sigma = 0.1$

Disclosures

The authors declare that they have no competing interests.

References

1. H. C. van de Hulst and J. J. M. Reesinck, "Line Breadths and Voigt Profiles," Astrophys. J. **106**, 121 (1947).
2. L. Galatry, "Simultaneous effect of doppler and foreign gas broadening on spectral lines," Phys. Rev. **122**(4), 1218–1223 (1961).
3. S. G. Rautian and I. I. Sobel'man, "The effect of collisions on the doppler broadening of spectral lines," Sov. Phys. Usp. **9**(5), 701–716 (1967).
4. A. R. Stokes, "A numerical fourier-analysis method for the correction of widths and shapes of lines on x-ray powder photographs," Proc. Phys. Soc. **61**(4), 382–391 (1948).
5. A. J. C. Wilson, "Variance as a measure of line broadening," Nature **193**(4815), 568–569 (1962).
6. T. H. De Keijser, J. I. Langford, E. J. Mittemeijer, and A. B. P. Vogels, "Use of the voigt function in a single-line method for the analysis of x-ray diffraction line broadening," J. Appl. Crystallogr. **15**(3), 308–314 (1982).
7. H. Maletta, G. Aeppli, and S. M. Shapiro, "Spin correlations in nearly ferromagnetic $Eu_xSr_{1-x}S$," Phys. Rev. Lett. **48**(21), 1490–1493 (1982).
8. P. A. M. Dirac and N. H. D. Bohr, "The quantum theory of the emission and absorption of radiation," *Proc. Royal Soc. London. Ser. A, Containing Pap. a Math. Phys. Character* 114, 243–265 (1927).
9. H. Schober, "M. born, optik," Monatshefte für Mathematik und Physik **40**(1), A36–A37 (1933).
10. J. Orear and E. Fermi, *Nuclear physics: a course given by Enrico Fermi at the University of Chicago*. (University of Chicago Press, 1967), chap. ix, p. 248
11. S. Enzo, G. Fagherazzi, A. Benedetti, and S. Polizzi, "A profile-fitting procedure for analysis of broadened x-ray diffraction peaks. i. methodology," J. Appl. Crystallogr. **21**(5), 536–542 (1988).
12. I. H. Hutchinson, *Principles of Plasma Diagnostics* (Cambridge University Press, 2002), 2nd ed.
13. B. Shin, "A simple quasi-analytical method for the deconvolution of voigtian profiles," J. Magn. Reson. **249**, 1–8 (2014).
14. A. McLean, C. Mitchell, and D. Swanston, "Implementation of an efficient analytical approximation to the voigt function for photoemission lineshape analysis," J. Electron Spectrosc. Relat. Phenom. **69**(2), 125–132 (1994).

15. Y. Liu, J. Lin, G. Huang, Y. Guo, and C. Duan, "Simple empirical analytical approximation to the voigt profile," J. Opt. Soc. Am. B **18**(5), 666–672 (2001).
16. S. Abousahl, M. Gourma, and M. Bickel, "Fast fourier transform for voigt profile: Comparison with some other algorithms," Nucl. Instrum. Methods Phys. Res., Sect. A **395**(2), 231–236 (1997).
17. G. V. Vogman and U. Shumlak, "Deconvolution of stark broadened spectra for multi-point density measurements in a flow z-pinch," Rev. Sci. Instrum. **82**(10), 103504 (2011).
18. G. Matmon, S. A. Lynch, T. F. Rosenbaum, A. J. Fisher, and G. Aeppli, "Optical response from terahertz to visible light of electronuclear transitions in $LiYF_4:Ho^{3+}$," Phys. Rev. B **94**(20), 205132 (2016).
19. M. Planck, "Zur theorie des rotationsspektrums," Ann. Phys. **357**(5), 491–505 (1917).
20. G. Jung, H. Gude, and G. Jung, "Das rotationsschwingungsspektrum des gasförmigen, flüssigen und gelösten ammoniaks," Zeitschrift für Elektrochemie und angewandte physikalische Chemie **37**, 545–548 (1931).
21. S. Albert, K. Keppler Albert, and M. Quack, *High Resolution Fourier Transform Infrared Spectroscopy* (Wiley, 2011), p. 1019. Published online 15 September 2011.
22. T. Chatterji, M. Zamponi, and J. Wuttke, "Hyperfine interaction in cobalt by high-resolution neutron spectroscopy," J. Phys.: Condens. Matter **31**(2), 025801 (2019).
23. J. M. Vandenberg, R. A. Hamm, M. B. Panish, and H. Temkin, "High-resolution x-ray diffraction studies of InGaAs(P)/InP superlattices grown by gas-source molecular-beam epitaxy," J. Appl. Phys. **62**(4), 1278–1283 (1987).
24. T. W. Hänsch, "Nobel lecture: Passion for precision," Rev. Mod. Phys. **78**(4), 1297–1309 (2006).
25. M. A. Foster, J. S. Levy, O. Kuzucu, K. Saha, M. Lipson, and A. L. Gaeta, "Silicon-based monolithic optical frequency comb source," Opt. Express **19**(15), 14233–14239 (2011).
26. W. Ruland, "The separation of line broadening effects by means of line-width relations," J. Appl. Crystallogr. **1**(2), 90–101 (1968).
27. M. V. Klein and T. E. Furtak, *Optics* (Wiley, 1986), chap. 6, pp. 293–304.
28. J. Olivero and R. Longbothum, "Empirical fits to the voigt line width: A brief review," J. Quant. Spectrosc. Radiat. Transfer **17**(2), 233–236 (1977).
29. S. Albert, K. K. Albert, P. Lerch, and M. Quack, "Synchrotron-based highest resolution fourier transform infrared spectroscopy of naphthalene (C10H8) and indole (C8H7N) and its application to astrophysical problems," Faraday Discuss. **150**, 71–99 (2011).
30. J. Als-Nielsen and D. McMorrow, *Kinematical scattering II: crystalline order* (John Wiley & Sons, Ltd, 2011), chap. 5, pp. 147–205.
31. M. Holler, M. Guizar-Sicairos, E. H. R. Tsai, R. Dinapoli, E. Müller, O. Bunk, J. Raabe, and G. Aeppli, "High-resolution non-destructive three-dimensional imaging of integrated circuits," Nature **543**(7645), 402–406 (2017).
32. M. Holler, M. Odstrcil, M. Guizar-Sicairos, M. Lebugle, E. Müller, S. Finizio, G. Tinti, C. David, J. Zusman, W. Unglaub, O. Bunk, J. Raabe, A. F. J. Levi, and G. Aeppli, "Three-dimensional imaging of integrated circuits with macro- to nanoscale zoom," Nat. Electron. **2**(10), 464–470 (2019).
33. F. J. Harris, "On the use of windows for harmonic analysis with the discrete fourier transform," Proc. IEEE **66**(1), 51–83 (1978).
34. A. Nuttall, "Some windows with very good sidelobe behavior," IEEE Trans. Acoust., Speech, Signal Process. **29**(1), 84–91 (1981).